

## Chapter 12

# Time Reversal of Linear and Nonlinear Water Waves

**A. Chabchoub,<sup>a,b</sup> A. Maurel,<sup>c</sup> V. Pagneux,<sup>d</sup> P. Petitjeans,<sup>e</sup>  
A. Prasadka,<sup>e</sup> and M. Fink<sup>c</sup>**

<sup>a</sup>*Department of Ocean Technology Policy and Environment, Graduate School of Frontier Sciences, University of Tokyo, Kashiwa, Chiba 277-8563, Japan*

<sup>b</sup>*Department of Mechanical Engineering, School of Engineering, Aalto University, FI-02150 Espoo, Finland*

<sup>c</sup>*Institut Langevin; ESPCI Paris, PSL Research University; CNRS; UPMC-Paris 6, Sorbone University; Univ. UPD-Paris 7; 1 rue Jussieu, 75005 Paris, France*

<sup>d</sup>*Laboratoire d'Acoustique de l'Université du Maine, UMR CNRS 6613, Avenue Olivier Messiaen, 72085 Le Mans, France*

<sup>e</sup>*Physique et Mécanique des Milieux Hétérogènes; ESPCI Paris, PSL Research University; CNRS; UPMC-Paris 6, Sorbone University; Univ. UPD-Paris 7; 10 rue Vauquelin, 75005 Paris, France*

### 12.1 Introduction

Time reversal (TR) of acoustic, elastic, and electromagnetic waves has been extensively studied in recent years [1, 2]. In a standard TR experiment, waves generated by a source are first measured by an array of antennas positioned around the source and then time-reversed and simultaneously rebroadcasted by the same

---

*Transformation Wave Physics: Electromagnetics, Elastodynamics, and Thermodynamics*

Edited by Mohamed Farhat, Pai-Yen Chen, Sebastien Guenneau, and Stefan Enoch

Copyright © 2016 Pan Stanford Publishing Pte. Ltd.

ISBN 978-981-4669-95-5 (Hardcover), 978-981-4669-96-2 (eBook)

[www.panstanford.com](http://www.panstanford.com)

antenna array. Due to the time invariance of the wave process, the reemitted energy will focus back on the original source, whatever the complexity of the propagation medium [3, 4]. The present paper concentrates on the application of TR to the focusing and manipulation of water waves both in linear and nonlinear regimes. The problem is not as trivial as that with acoustic waves. Let us cite Richard Feynman [5], “Water waves that are easily seen by everyone and which are usually used as an example of waves in elementary courses are the worst possible example, because they are in no respects like sound and light; they have all the complications that waves can have.” Water waves are scalar waves; that refers to the evolution of small perturbation of the height of fluid under the action of gravity and surface tension. They are dispersive by nature, nonlinear when generated with standard wave makers, and they experience strong damping at the scale of laboratory experiments. The effect of dispersion on the TR process has already been studied in TR experiments for guided elastic waves [6, 7]; these waves are dispersionless in free space, and the dispersion is due only to the reflection on the boundaries of the waveguide. In the case of water waves, the dispersion is intrinsic but preserves the TR invariance (obviously, not taking the damping into account). The effect of the nonlinearities has been experimentally studied in Ref. [8] for acoustic waves where it has been shown that the TR invariance is preserved as long as nonlinearities do not create dissipation, that is, as long as the propagation distance is smaller than the shock distance. In the case of water waves, the effect of nonlinearities has to be treated. The evolution dynamics in time and space of nonlinear wave trains in deep water can be modeled using the focusing nonlinear Schrödinger equation (NLSE). We will show the implication of the TR invariance on the NLSE and we will demonstrate a way to experimentally focus, both in time and space, rogue waves using the principles of TR mirrors.

## 12.2 Surface Gravity Water Waves

In this chapter the mathematical and physical preliminaries on water waves are introduced. It relies on the many excellent monographs that exist on the subject, see for instance [9–14].

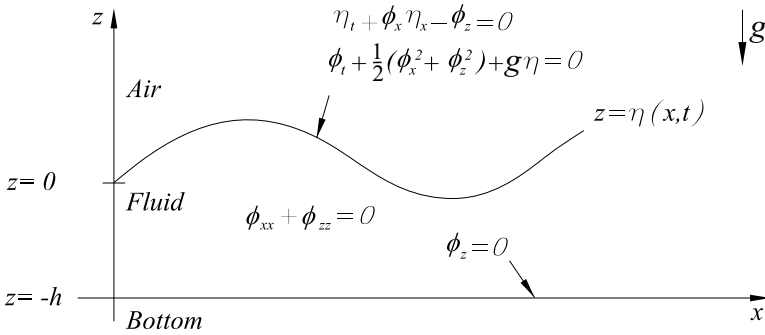


**Figure 12.1** Water waves with elevation perturbation  $\eta$  around  $z = 0$  and bottom at  $z = -h(x, y)$ .

We consider the propagation of water waves with local depth  $h(x, y)$  for a fluid at rest (Fig. 12.1). We start with the incompressible flow assumption. There are two criteria to be satisfied to assume incompressibility: low Mach number and a timescale associated to the flow much smaller than the sound timescale. The first is obviously highly justified in the context of water waves, since the velocity of the fluid is much smaller than the speed of sound in water  $c_{\text{sound}} \simeq 1500$  m/s. The timescale associated to water wave propagation scales as the inverse of the wave speed  $c_w$ , so that the second condition reads  $c_w/c_{\text{sound}} \ll 1$ ; as we will see later  $c_w \leq \sqrt{gh}$  with  $g$  the gravity constant, which tell us that it is sufficient to have  $h < 200$  km to assume incompressibility, which is evidently always verified [9].

For incompressible flows, Navier–Stokes equations take the form

$$\begin{cases} \frac{\partial \mathbf{u}}{\partial t} + \mathbf{u} \nabla \mathbf{u} = -\frac{1}{\rho} \nabla P + \mathbf{g} + \nu \Delta \mathbf{u}, \\ \nabla \mathbf{u} = 0, \end{cases} \quad (12.1)$$

where  $\nu = \mu/\rho$  is the kinematic viscosity. Here, we also assume a small effect of the viscosity. This means that we neglect the condition of no slip at the bottom  $z = -h$  and that we neglect the shear stress at the free surface  $z = \eta$ . These boundary layer effects would be a correction responsible of the wave damping [9, 10].

Next, introducing the vorticity  $\boldsymbol{\omega} = \nabla \times \mathbf{u}$ , we get the Euler equation

$$\begin{cases} \frac{\partial \mathbf{u}}{\partial t} + \nabla \left( \frac{\mathbf{u}^2}{2} \right) - \mathbf{u} \times \boldsymbol{\omega} = -\frac{1}{\rho} \nabla P + \mathbf{g} + \nu \Delta \mathbf{u}, \\ \nabla \mathbf{u} = 0, \end{cases} \quad (12.2)$$

If we assume that the flow is initially irrotational  $\boldsymbol{\omega}(t = 0) = 0$ , Kelvin's theorem ensures that the flow remains irrotational for subsequent time. This allows to define a velocity potential  $\phi(\mathbf{x}, t)$  such that

$$\mathbf{u} = \nabla \phi. \quad (12.3)$$

Euler equations simplify into

$$\begin{cases} \nabla \left( \frac{\partial \phi}{\partial t} + \frac{\mathbf{u}^2}{2} + \frac{P}{\rho} + gz \right) = 0, \\ \nabla \mathbf{u} = \Delta \phi = 0. \end{cases} \quad (12.4)$$

The first equation in Eq. 12.4 leads to the Bernoulli equation

$$\frac{\partial \phi}{\partial t} + \frac{\mathbf{u}^2}{2} + \frac{P}{\rho} + gz = F(t) \quad (12.5)$$

Next, because only the gradient of  $\phi$  has a physical meaning, it can be shifted by any function of time. Thus, applying Eq. 12.5 at the free surface and the shift  $\phi \rightarrow \phi + P_0 t/\rho - \int dt F(t)$ , with  $P_0$  the ambient atmospheric pressure, we get

$$\frac{\partial \phi}{\partial t} + \frac{\mathbf{u}^2}{2} + g\eta = 0, \quad \text{at } z = \eta. \quad (12.6)$$

Two other boundary conditions have to be accounted for. The first is at the free surface  $z = \eta$  and it links the motion of the free surface to the velocity of the fluid. To do this, we use the principle that "what happens at the free surface stays at the free surface." More precisely, the free surface  $F(\mathbf{x}, t) = z - \eta(x, y, t) = 0$  is assumed to be a material surface, yielding  $(\partial_t + (\mathbf{u} \cdot \nabla)) F = 0$ . Then, using  $(\partial_t + (\mathbf{u} \cdot \nabla)) z = v_z = \partial_z \phi$ , we obtain

$$\partial_z \phi = \partial_t \eta + \partial_x \phi \partial_x \eta + \partial_y \phi \partial_y \eta, \quad \text{at } z = \eta. \quad (12.7)$$

The boundary condition at the bottom is the most straightforward to obtain. Since we neglect the viscous boundary layer, it simply states

that there is no normal velocity (nonpenetrable condition)

$$\mathbf{n} \times \nabla\phi = 0, \quad \text{at } z = -h, \tag{12.8}$$

with  $\mathbf{n}$  the vector normal to the bottom  $z = -h$ .

Eventually, the problem to be solved is reduced to

$$\begin{cases} \Delta\phi = 0, & \text{in the bulk,} \\ \partial_t\phi + \frac{\mathbf{u}^2}{2} + g\eta = 0, & \text{at } z = \eta, \\ \partial_z\phi = \partial_t\eta + \partial_x\phi \partial_x\eta + \partial_y\phi \partial_y\eta, & \text{at } z = \eta, \\ \mathbf{n} \times \nabla\phi = 0, & \text{at } z = -h(x, y). \end{cases} \tag{12.9}$$

### 12.2.1 Linear Approximation

Here, we denote  $k = 2\pi/\lambda$  with  $\lambda$  the typical wavelength of the water waves,  $a$  the typical wave amplitude and  $H$  the typical depth scale. Linear approximation is submitted to the condition of small generalized Ursell number [11]

$$U_r = \frac{ka}{\tanh(kh)^3} \ll 1. \tag{12.10}$$

In the shallow water approximation,  $kh \ll 1$ , it becomes the Ursell number, and in the deep water approximation,  $kh \gg 1$ , it becomes simply the sea slope or steepness  $ka$ . Below, we present the water wave equations for transient behaviors (time domain) and for forced behaviors (harmonic regime in the frequency domain).

#### 12.2.1.1 Equations in the time domain

For transient behaviors we keep the time differentiation. Due to linear approximation, the system (12.9) is simplified into

$$\begin{cases} \Delta\phi = 0, & \text{in the bulk,} \\ \partial_t\phi + g\eta = 0, & \text{at } z = 0, \\ \partial_z\phi = \partial_t\eta, & \text{at } z = 0, \\ \mathbf{n} \times \nabla\phi = 0, & \text{at } z = -h(x, y), \end{cases} \tag{12.11}$$

where the explicit nonlinear terms have been suppressed and where the boundary condition at  $z = \eta$  has been linearized to  $z = 0$ . This system can be arranged in terms of  $\phi$  only

$$\begin{cases} \Delta\phi = 0, & \text{in the bulk,} \\ \partial_{tt}\phi + g\partial_z\phi = 0, & \text{at } z = 0, \\ \mathbf{n} \times \nabla\phi = 0, & \text{at } z = -h(x, y). \end{cases} \quad (12.12)$$

### 12.2.1.2 Harmonic regime and flat bottom

In the harmonic regime, the time dependence is written  $\exp(-i\omega t)$  and it will be omitted in the following equation. For a flat bottom, the depth is a constant  $h(x, y) = h$ , and the boundary condition at the bottom become  $\partial_z\phi = 0$ , so that the system (12.13) becomes

$$\begin{cases} \Delta\phi = 0, & \text{in the bulk,} \\ \partial_z\phi = \frac{\omega^2}{g}\phi, & \text{at } z = 0, \\ \partial_z\phi = 0, & \text{at } z = -h. \end{cases} \quad (12.13)$$

In this simple case, we can look for a modal solution in the form  $\phi(x, y, z) = \exp(i\mathbf{k}\mathbf{x}) f(z)$ , where  $\mathbf{x}$  denotes now the horizontal position vector  $\mathbf{x} = (x, y)$ . In what follows, we consider a 1D propagation, and the function  $f$  is found to satisfy

$$f'' - k^2 f = 0, \quad \text{with } f'(-h) = 0, \text{ and } f'(0) = \frac{\omega^2}{g} f(0). \quad (12.14)$$

The dispersion relation that comes from this eigenvalue problem is

$$\omega^2 = gk \tanh kh. \quad (12.15)$$

The associated eigenfunctions are of the form  $f(z) = \cosh k(z + h)$ . For a given frequency, the dispersion relation has one real solution associated to propagating surface waves and an infinity of imaginary solutions associated to evanescent waves.

Deep-water waves are characterized by having small wavelengths compared to the water depth, that is,  $kh \gg 1$ . Since for this case  $\tanh kh \approx 1$ , the linear dispersion relation for deep-water waves is

$$\omega = \sqrt{gk}. \quad (12.16)$$

Hence, the phase velocity of the waves is

$$c_{pd} = \frac{\omega}{k} = \sqrt{\frac{g}{k}}, \tag{12.17}$$

while the regular surface elevation of amplitude  $a$ , a wave frequency of  $\omega$ , and a wave number of  $k$  is determined by

$$\eta(x, t) = a \cos(kx - \omega t). \tag{12.18}$$

Moreover, slowly modulated deep-water periodic-wave train envelopes propagate with the group velocity

$$c_g = \frac{d\omega}{dk} = \frac{1}{2} \sqrt{\frac{g}{k}} = \frac{\omega}{2k} = \frac{1}{2} c_{pd}. \tag{12.19}$$

For the deep-water case, it is possible to approximate the evolution of linear wave packets within the framework of envelope evolution equation. The latter can be derived heuristically by expanding the dispersion relation (Eq. 12.16) about  $k = k_0$  [15, 16]

$$\omega(k) = \omega(k_0) + \left(\frac{\partial\omega}{\partial k}\right)(k - k_0) + \frac{1}{2}(k - k_0)^2 \left(\frac{\partial^2\omega}{\partial k^2}\right) \Big|_{k=k_0}. \tag{12.20}$$

Now, we define the slowly varying wave number and wave frequency to be  $K := k - k_0$  and  $\Omega = \omega - \omega_0$ , respectively. Thus, Eq. 12.20 becomes

$$\Omega - \left(\frac{\partial\omega}{\partial k}\right) K - \frac{1}{2} K^2 \left(\frac{\partial^2\omega}{\partial k^2}\right) \Big|_{k=k_0} = 0. \tag{12.21}$$

Applying the Fourier transform gives

$$E(K, \Omega) = \mathcal{F}[E(x, t)] = \int_{-\infty}^{+\infty} E[x, t] \exp[i(\Omega t - Kx)] dx dt, \tag{12.22}$$

while the inverse Fourier transform provides

$$\begin{aligned} E(x, t) &= \mathcal{F}^{-1}[E(K, \Omega)] \\ &= \frac{1}{(2\pi)^2} \int_{-\infty}^{+\infty} E[K, \Omega] \exp[-i(\Omega t - Kx)] dK d\Omega, \end{aligned} \tag{12.23}$$

It is straightforward to verify from Eqs. 12.22 and 12.23 that

$$E_x = iK\mathcal{F}^{-1}[E(K, \Omega)]; \quad E_t = -i\Omega\mathcal{F}^{-1}[E(K, \Omega)]; \tag{12.24}$$

Applying the operator (Eq. 12.21) on the envelope function  $E$  and using the derivative expression (Eq. 12.24), we obtain its linear evolution dynamics in space and time

$$-i \left( E_t + \frac{\omega}{2k} E_x \right) + \frac{\omega}{8k^2} E_{xx} = 0. \quad (12.25)$$

Equation 12.25 is also referred to as the linear Schrödinger equation. For a given linear solution of Eq. 12.25, the corresponding surface elevation to first order of approximation is determined by

$$\eta(x, t) = \text{Re} ( E (x, t) \cdot \exp [i (kx - \omega t)] ). \quad (12.26)$$

For shallow-water waves, the wavelength is large compared with the water depth. Therefore,  $kh \ll 1$ . Hence,  $\tanh kh \approx kh$ , which means that the dispersion relation for shallow-water waves is

$$\omega = \sqrt{gk^2 h}. \quad (12.27)$$

Then, the phase velocity is

$$c_{\text{ps}} = \frac{\omega}{k} = \sqrt{gh}. \quad (12.28)$$

Since shallow-water waves are nondispersive, the group velocity is equal to the phase velocity.

Whatever the depth (deep water, shallow water, or intermediate depth) the phase velocity is

$$c_{\text{ps}} = \frac{\omega}{k} = \sqrt{gh} \sqrt{\frac{\tanh kh}{kh}}. \quad (12.29)$$

Then, since  $\tanh a \leq a$ , it shows that the shallow-water expression of the phase velocity is a maximum, in the sense that we always have

$$c_{\text{ps}} \leq \sqrt{gh}. \quad (12.30)$$

### 12.2.1.3 2D equation in the harmonic regime for a flat bottom

The vertical mode that we have defined previously is useful to obtain a 2D equation for water waves, analogous to the Helmholtz 2D equation for acoustic waves. We know from (12.13) that the equation for the potential in the bulk is

$$\frac{\partial^2 \phi}{\partial x^2} + \frac{\partial^2 \phi}{\partial y^2} + \frac{\partial^2 \phi}{\partial z^2} = 0. \quad (12.31)$$

Thus, for a geometry that is separable in  $(x, y)$  and  $z$ , it is possible to decompose the potential  $\phi$  with the vertical mode  $f(z)$  by writing

$$\phi(x, y, z) = f(z)\Psi(x, y).$$

Then, from the previous equation, we obtain

$$\frac{\partial^2 \Psi}{\partial x^2} + \frac{\partial^2 \Psi}{\partial y^2} + k^2 \Psi = 0. \quad (12.32)$$

This is the 2D Helmholtz equation and it is exact—in the linear regime—for separable geometries, that is, with a flat bottom and lateral vertical walls. The boundary conditions at these vertical walls correspond to vanishing normal velocity and thus to

$$\partial_n \Psi = 0. \quad (12.33)$$

Besides, the relation between the potential at the surface and the elevation perturbation,  $\partial_z \phi(x, y, 0) = -i\omega\eta(x, y)$ , allows us to express the 2D problem for  $\eta$ :

$$\frac{\partial^2 \eta}{\partial x^2} + \frac{\partial^2 \eta}{\partial y^2} + k^2 \eta = 0 \quad (12.34)$$

with Neumann boundary conditions on the vertical walls

$$\frac{\partial \eta}{\partial n} = 0. \quad (12.35)$$

Eventually, it appears that, in the harmonic regime for separable geometries, there is a perfect analogy between water waves and acoustic waves (as well as with transverse electromagnetic waves).

#### 12.2.1.4 Time reversal invariance in the linear regime

From the previous considerations that have shown the analogy with 2D acoustics we can conclude immediately that water waves possess the TR invariance when the geometry is separable.

However, there is simpler and more general argument. We remind the linear equations in the time domain

$$\begin{cases} \Delta \phi = 0, & \text{in the bulk,} \\ \partial_{tt} \phi + g \partial_z \phi = 0, & \text{at } z = 0, \\ \mathbf{n} \cdot \nabla \phi = 0, & \text{at } z = -h(x, y). \end{cases} \quad (12.36)$$

It is valid in any geometry, with any shape of the bottom, and it is obviously invariant with respect to the symmetry  $t \rightarrow -t$ . It means that linear water waves are TR invariant in any geometry (as long as the damping is neglected).

### 12.2.2 Nonlinear Regime

The propagation of nonlinear waves in one spatial dimension and in deep-water condition can be described within the framework of weakly nonlinear Stokes waves [17]. These waves have the property to have flatter troughs and sharper peaks. Another fundamental property is their instability to side-band perturbation [18]. The dynamics of these waves in both, stationary and unstable regime can be accurately described by nonlinear Schrödinger-type evolution equations [19, 20]. Being an integrable evolution equation, exact envelope model solutions of the NLSE can be used to model exact localized structures on the water surface [21].

#### 12.2.2.1 Stokes waves and modulation instability

Using the perturbation Ansatz in the small steepness parameter  $\varepsilon := ka$ , Stokes found weakly nonlinear periodic solutions, which satisfy the nonlinear governing equations of an ideal fluid [17]. The weakly nonlinear surface elevation to second order in steepness is determined by

$$\eta(x, t) = a \cos(kx - \omega t) + \frac{1}{2}ka^2 \cos[2(kx - \omega t)] + \dots \quad (12.37)$$

The dispersion relation is then corrected to

$$\omega = \sqrt{gk} \left( 1 + \frac{a^2 k^2}{2} \right). \quad (12.38)$$

Considering the corrected dispersion relation (Eq. 12.38), we can notice the dependency of the wave velocity with respect to the amplitude. This amplitude dependency may engender a nonlinear focusing of Stokes waves under certain conditions. This instability of periodic deep-water wave trains is also referred to as the Benjamin-Feir instability [18], the side-band instability or the Bespalov-Talanov instability [22]. This instability has been discovered at the same time by various researcher [12]. A geometric condition for the instability was already provided by Lighthill [9]. Benjamin and Feir [18] investigated the stability of Stokes waves theoretically and experimentally, while Zakharov [19] derived the same result using a Hamiltonian approach. In the same work he derived an equation,

which describes the evolution in time and space of slowly modulated weakly nonlinear wave trains in deep water, the NLSE, which will be discussed in the next section. Benjamin and Feir examined the second-order Stokes solution to side-band disturbances [18, 23, 28], where the disturbed surface elevation has the form

$$\tilde{\eta}(x, t) = \eta(x, t) + \epsilon(x, t), \quad (12.39)$$

while the side-band disturbance is given by

$$\begin{aligned} \epsilon(x, t) = & \epsilon_+ \exp(\gamma t) \cos[k(1 + \kappa)x - \omega(1 + \delta)t] + \\ & \epsilon_- \exp(\gamma t) \cos[k(1 - \kappa)x - \omega(1 - \delta)t]. \end{aligned} \quad (12.40)$$

Here,  $\epsilon_{\pm}$  denote small amplitudes of the perturbation, whereas  $\delta = \Omega/\omega$  and  $\kappa = K/k$  are small perturbations fractions of the wave frequency and wave number, respectively. After substitution of the perturbed wave equation  $\tilde{\eta}(x, t)$  in the governing equations (11) and performing a linear stability analysis of the obtained dynamical system provides to the instability growth rate

$$\gamma = \frac{1}{2} \delta \sqrt{2k^2 a^2 - \delta^2 \omega} \quad (12.41)$$

Therefore, the disturbances grow exponentially with time for real values of  $\gamma$ . That is, whenever  $\gamma$  is real, the instability exists in a limited range of modulation frequencies:

$$0 < \delta < \sqrt{2}ka. \quad (12.42)$$

Therefore, for a given wave steepness  $\varepsilon$  of a regular deep-water wave train, there exists an unstable frequency range, centered around the main frequency  $\omega$ , for which the growth rate  $\gamma$  is real and positive. In this case, disturbances grow exponentially with time. The side-band instability was also experimentally observed in a large wave facility shortly after its theoretical discovery [24, 25].

#### 12.2.2.2 Nonlinear Schrödinger equation and doubly localized breather-type solutions

An alternative to describe the exact dynamics of Stokes waves is provided by the theory of nonlinear wave packet evolution equations. The simplest equation for nonlinear wave packets of this type is known as the NLSE and can be derived heuristically by

extending the results Taylor expansion, presented for the linear case, by including the dependency of the dispersion relation with respect to the amplitude, as described in Eq. 12.38. That is,

$$\begin{aligned} \omega(k) = \omega(k_0) + \left(\frac{\partial\omega}{\partial k}\right)(k - k_0) + \frac{1}{2}(k - k_0)^2 \left(\frac{\partial^2\omega}{\partial k^2}\right)\Big|_{k=k_0} \\ + \left(\frac{\partial\omega}{\partial |a|^2}\right)\Big|_{|a|^2=0} |a|^2. \end{aligned} \quad (12.43)$$

Therefore, Eq. 12.25 is corrected to

$$-i \left(E_t + \frac{\omega}{2k} E_x\right) + \frac{\omega}{8k^2} E_{xx} + \frac{\omega k^2}{2} |E|^2 E = 0, \quad (12.44)$$

which the NLSE. Now, weakly nonlinear surface elevation to first order of approximation is determined by

$$\eta(x, t) = \text{Re} \left( E(x, t) \cdot \exp[i(kx - \omega t)] \right). \quad (12.45)$$

The latter equation can be derived more rigorously from the governing equations, using the multiple scales technique, see [10, 26]. The interesting fact about the NLSE, is that its stationary solution  $E_S(x, t) = a \exp\left(-i \frac{a^2 k^2}{2} \omega t\right)$  describes a second-order Stokes waves and same instability condition (Eq. 12.42) can be derived, by perturbing the stationary Stokes envelope  $E_S(x, t)$  by a modulation frequency  $\Omega$  and a modulation wave number  $K$ . Therefore, the considered perturbed envelope function becomes

$$\begin{aligned} \tilde{E}_S(x, t) = E_S(x, t) \left[ 1 + \varepsilon_- \exp\left(-i K \left(x - \frac{\omega}{2k} t\right) - i \Omega t\right) + \right. \\ \left. \varepsilon_+ \exp\left(i K \left(x - \frac{\omega}{2k} t\right) + i \Omega t\right) \right]. \end{aligned} \quad (12.46)$$

The criterion (Eq. 12.42) is then obtained after inserting the perturbed Stokes envelope in the NLSE, linearizing and following the modulation dispersion relation

$$\Omega^2 = \frac{\omega^2}{8k^2} \left( \frac{K}{8k^2} - k^2 a^2 \right) K^2, \quad (12.47)$$

see [10, 11, 27] for details. An exponential growth takes place, when the modulation frequency is imaginary. This is the case, when

$$0 < \frac{K}{k} < 2\sqrt{2}ka. \quad (12.48)$$

Since for deep water  $c_g = \frac{\Omega}{K} = \frac{\omega}{2k}$ , thus,  $\delta = \frac{\Omega}{\omega} = \frac{1}{2} \frac{K}{k} = \frac{1}{2} \kappa$ , Eq. 12.48 is clearly equivalent to Eq. 12.42. The modulation instability can be discussed within the framework of exact solutions of the NLSE. Besides stationary wave envelope soliton solutions, the NLSE admits a family of breather solution on a constant Stokes background, known to model strong localizations of Stokes waves [29–33]. For simplicity, we scale the NLSE to a dimensional form [12]

$$i \psi_T + \psi_{XX} + 2 |\psi|^2 \psi = 0. \quad (12.49)$$

The solution, which describes the modulation instability dynamics in space and time is the family of space-periodic Akhmediev solutions [29], expressed as

$$\psi_A(X, T) = \frac{\cosh(\Omega T - 2i\varphi) - \cos(\varphi) \cos(pX)}{\cosh(\Omega T) - \cos(\varphi) \cos(pX)} \exp(2iT), \quad (12.50)$$

where  $\Omega = 2 \sin(2\varphi)$ ,  $p = 2 \sin(\varphi)$  and  $\varphi \in \mathbb{R}$ . In the limiting case of infinite modulation period, which occurs when the breather parameter  $\varphi \rightarrow 0$ , is known as the Peregrine solution [33]

$$\psi_1(X, T) = \left( -1 + \frac{4 + 16iT}{1 + 4X^2 + 16T^2} \right) \exp(2iT), \quad (12.51)$$

Here, the modulation wavelength  $K \approx 0$  and the growth rate becomes algebraic and is not of exponential nature anymore. This latter solution is very particular, since it is localized in both space and time and it amplifies the amplitude of the carrier theoretically by an exact factor of three. A higher-order solution of this kind is referred to as the Akhmediev–Peregrine solution [29, 34, 35]. This doubly localized solution is characterized by a maximal amplitude amplification of five (see Fig. 12.2 for an illustration) and is defined by

$$\psi_2(X, T) = \left( 1 + \frac{G + iH}{D} \right) \exp(2iT), \quad (12.52)$$

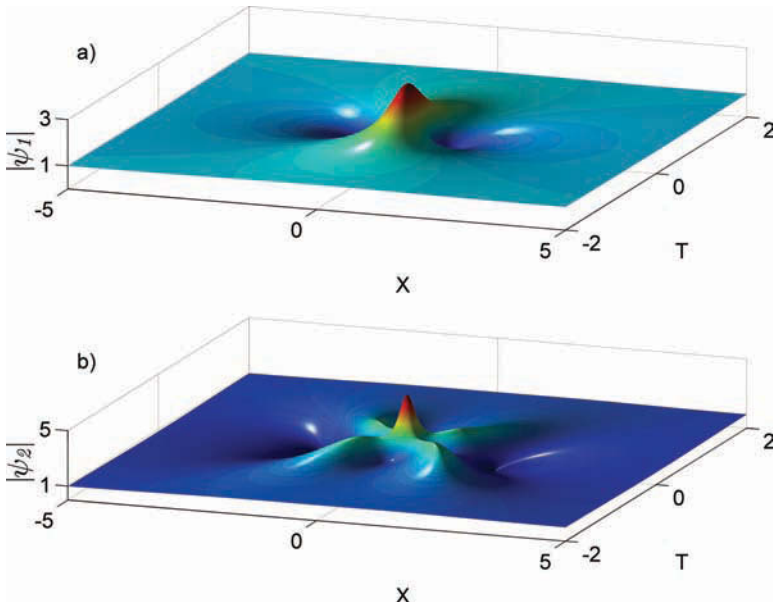


**Figure 12.2** (a) First-order doubly localized rational solution (Peregrine breather), which at  $X = T = 0$  amplifies the amplitude of the carrier by a factor of 3. (b) Second-order doubly localized rational solution (Akhmediev-Peregrine breather), which at  $X = T = 0$  amplifies the amplitude of the carrier by a factor of 5.

while

$$G = - \left( X^2 + 4T^2 + \frac{3}{4} \right) \left( X^2 + 20T^2 + \frac{3}{4} \right) + \frac{3}{4} \quad (12.53)$$

$$H = 2T \left( 3X^2 - 4T^2 - 2(X^2 + 4T^2)^2 + \frac{15}{8} \right) \quad (12.54)$$

$$D = \frac{1}{3} (X^2 + 4T^2)^3 + \frac{1}{4} (X^2 - 12T^2)^2 + \frac{3}{64} (12X^2 + 176T^2 + 1). \quad (12.55)$$

All these basic breather solutions, which describe the strong focusing of a regular background have been only recently observed in Kerr media, water waves and plasma [36–42]. Breathers attracted the significant scientific interest, since they describe the backbone dynamics of the modulation instability and therefore, of rogue wave as well.

### 12.2.2.3 Time reversal invariance in the nonlinear regime

The TR invariance of Stokes waves can be discussed within the framework of the NLSE. In fact, considering the weakly nonlinear evolution equation (Eq. 12.44), we can notice that the time-dependent part of the NLSE equation, contains a term in  $i \frac{\partial E}{\partial t}$ . Therefore, it is straightforward to see that if  $E(x, t)$  is a solution, then its complex conjugate  $E^*(x, -t)$  is also a solution. Consequently, both surface elevations  $\eta(x, t)$  and  $\eta(x, -t)$  describe two possible evolutions for the weakly nonlinear water wave problem. Consequently, a TR mirror can be used to create the time-reversed wave field  $\eta(x, -t)$  in the whole propagating medium. For this 1D problem it is sufficient to measure the wave field  $\eta(x, t)$  at one unique point  $x_M$  and to rebroadcast the time-reversed signal  $\eta(x_M, -t)$  from this mirror point in order to observe the solution  $\eta(x, -t)$  in the whole medium. If this approach is valid for breather dynamics, it would be a confirmation of the TR invariance of strongly localized waves and therefore for nonlinear waves as well.

## 12.3 Experiments of Time Reversal

In this section we describe recent experiments, confirming the TR invariance of linear [43] and nonlinear surface gravity waves [44].

### 12.3.1 Time Reversal of Linear Water Waves

In this section we will start reporting the results of the TR of water waves in the linear regime. The experiment is conducted in a water tank cavity to take advantage of multiple reflections on the boundaries. The influence of the number of channels in the TR mirror is studied and it allows us to show that a small number of channels is sufficient to obtain the TR refocusing owing to the reverberating effect of the cavity.

The reverberating tank is filled with water with depth at rest  $H = 10$  cm. The dimension of the rectangular tank is  $53 \times 38$  cm<sup>2</sup> with obstacles placed in order to break the spatial symmetries (see Fig. 12.3). The waves are generated by using a vertical conical vibrator and recorded by using an optical method (note that

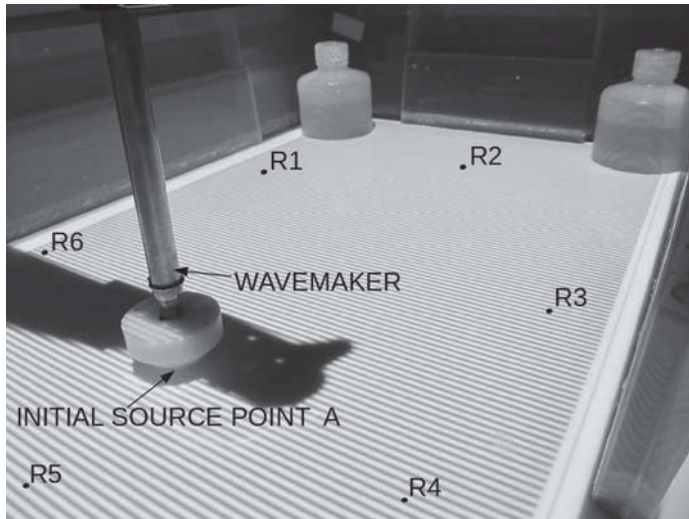


**Figure 12.3** Water tank used in the experiment. Point A is at the initial source position. Note the fringes used for the Fourier transform profilometry technique. Points  $R_1$  to  $R_6$  correspond to the positions of the different channels of the TR mirror. At each of these channel positions the wave is measured and can be reemitted after the TR operation. Reprinted (figure) with permission from Ref. [43]. Copyright (2012) by the American Physical Society.

this differs from TR experiments in acoustics that use the same transducer to record and to regenerate the wave). We perform a typical one channel TR experiments in two steps. In the first step of emission, a wave packet is generated from a conical vibrator that can be considered as a point source. In a second step, the signal recorded at a receiver point is time-reversed and reemitted.

The time-reversed wave is expected to refocus spatially at the source point and refocus temporally at the recompression time. The key point to ensure TR refocusing is the number of cavity modes that the wave packet has been able to excite in the first step of the TR.

After a few experimental trials, the authors found the central frequency  $f_0 = 5$  Hz the best to obtain good refocusing in time and space. This is a compromise between the bulk dissipation that grows with a frequency increase and the bottom friction that becomes significant while decreasing frequency (note: no significant

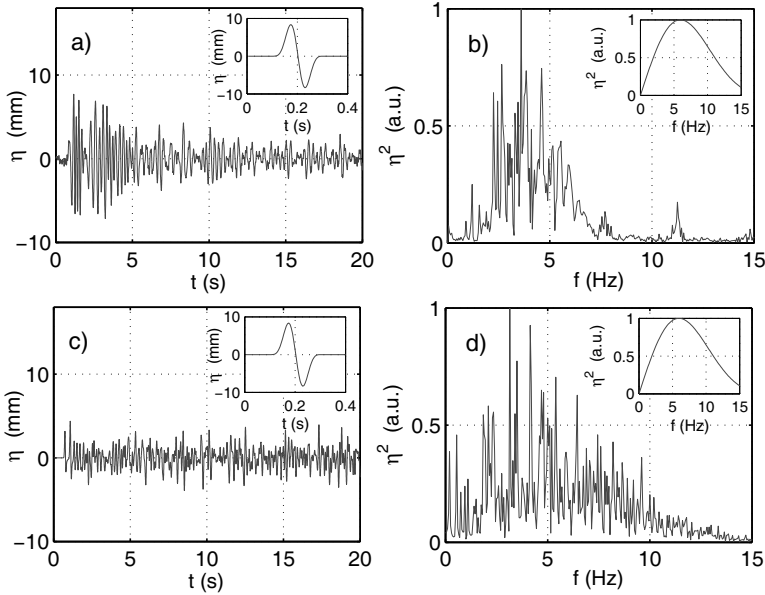


**Figure 12.4** (a) Experimental measurement of the temporal evolution of the surface elevation,  $\eta(\mathbf{r}_1, t)$  during the forward propagation after emission from point A. The inset shows the signal emitted from point A. (b) Corresponding spectrum. The inset shows the spectrum of the signal emitted from point A. (c, d) The same representation from numerical simulations of the wave equation. Reprinted (figure) with permission from Ref. [43]. Copyright (2012) by the American Physical Society.

peaks in the low-frequency region in Fig. 12.4b). Figure 12.4a shows the signal recorded at one point (point  $R_1$  in Fig. 12.3) when a one-period sinusoidal pulse centered at  $f_0$  Hz is generated at the initial source position. The duration of the signal is typically 20 s, corresponding both to reverberating effects and linear dispersion effects. This latter is given by the linear dispersion relation for water wave propagation (taking into account the effects of finite depth  $H$  and surface tension  $\gamma$ ):

$$\omega^2 = \left( gk + \frac{\gamma}{\rho} k^3 \right) \tanh kH, \quad (12.56)$$

where  $k$  denotes the complex wave number,  $g$  the gravity acceleration and  $\rho$  the water density. The wavelength at the central

frequency  $f_0$  is  $\lambda = 6$  cm. The magnitude of nonlinearity of the waves based on the maximum measured gradient of surface elevation was found to be  $\epsilon = 0.13$ . The attenuation is such that the wave can propagate over roughly 100 wavelengths, that is, about 10 to 20 times the length scale of the cavity. This is consistent with the 20 s duration of the time signal recorded at one point in the cavity (Fig. 12.4a) since the phase velocity at the central frequency is 0.33 m/s corresponding to 12–17 reflections from the boundaries. The spectrum of the signal recorded during the direct propagation is shown in Fig. 12.4b. It presents several peaks (one can count roughly 20 peaks) corresponding to the eigenmodes of the cavity that have been excited. Although the initial pulse covers a broadband frequency range [0 15] Hz, the signal recorded is limited to frequencies smaller than about 10 Hz. We have checked that this is an effect of the attenuation: direct numerical simulations of the 2D wave equation in the same geometry but omitting the attenuation give a spectrum with around 100 cavity modes excited in the whole range 0 15 Hz (Fig 12.4c,d).

We now investigate the refocusing. The perturbation of the surface elevation  $\eta(\mathbf{r}, t)$  is measured in time and in space during the wave propagation using an optical method (FTP for Fourier transform profilometry) that has been adapted recently to water wave measurements [45–48]. FTP is used to measure the whole pattern of surface elevation  $\eta(\mathbf{r}, t)$  at *each time* of the reverse propagation. This has been done in one-channel experiments ( $N = 1$ ). Although the spatial refocusing and temporal recompression are visible (Fig. 12.5), it is not possible to distinguish the converging wave fronts before the recompression and the diverging wave fronts after recompression in this one channel experiments (for a movie, see the supplementary material).

To improve the refocusing, it is possible to increase the number of channels. In a TR experiments with multiple channels, the signal emitted from the source point is recorded at  $N$  receiver points. The TR signal are then reemitted simultaneously from the  $N$  receiver points. If the  $N$  receiver points are uncorrelated, it is meant to improve the refocusing since the wave experiences many different trajectories in the cavity. In our experiment, rather than using  $N$  wave generators to reemit the signal, the  $N$  channel TR have been done with just one wave generator. This is possible by exploiting the

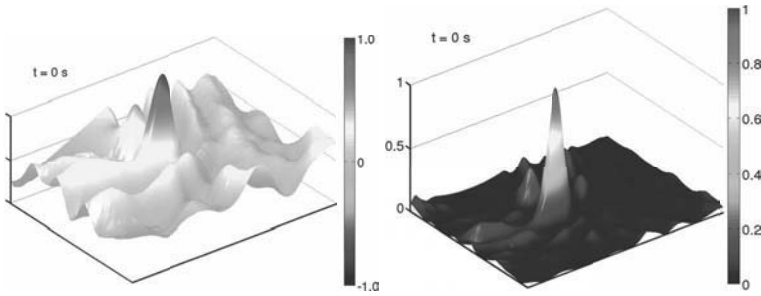


**Figure 12.5** Measured amplitude,  $\eta(\mathbf{r}, t = 0)$ , and intensity,  $\eta(\mathbf{r}, t = 0)^2$  of the time-reversed wave around the initial source position (point A) where the wave is refocused at the recompression time ( $t = 0$ ) in a one-channel TR experiment ( $N = 1$ ). The spatial range around the refocusing point A is  $34 \times 26 \text{ cm}^2$ . Reprinted (figure) with permission from Ref. [43]. Copyright (2012) by the American Physical Society.

linearity of the problem which implies that the wave field excited by  $N$  generators is equal to the sum of the  $N$  wave fields excited by each generator alone. We have checked this linearity by comparing the time signal recorded at the refocalization point when using 2 channels and when summing the two signals obtained in two single channel experiments (see supplementary material). The temporal signals in both cases coincide, with less than 10% discrepancy in a  $10/f_0$  time window centered at the recompression time. Six different positions of the receiver point have been used (points  $R_1$  to  $R_6$  in Fig. 12.3). Figure 12.6 shows a time sequence of the reverse propagation for the 6 channel TR. As expected, the peak at the recompression time is much higher than in the one channel TR, confirming that the channels are uncorrelated. Besides, the converging and diverging wave fronts, before and after the recompression time are visible.

To gain insights into the study of the quality of the refocusing, we want to inspect both the effect of the number of channels and the effect of the damping. To characterize the quality of the spatial refocusing, we define a peak-to-noise ratio (PNR) at the recompression time as the ratio of the maximum intensity at the focal spot to the mean side-lobe intensity. Experimental results are shown in Fig. 12.7 (black points). With a single channel, the PNR is typically 20, a value that is related to the number of cavity modes that can be resolved from the spectrum at the receiver

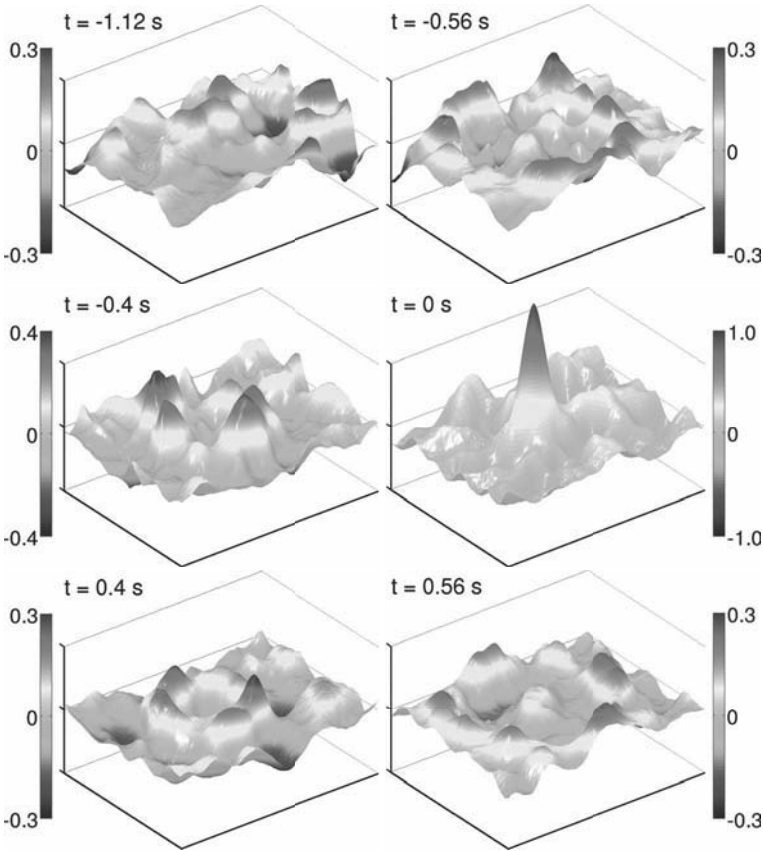


**Figure 12.6** Space-time-resolved experimental measurements of the surface elevation  $\eta(\mathbf{r}, t)$  during the refocusing of the time-reversed wave. In this case,  $N = 6$  channels (points  $R_1$  to  $R_6$ ) reemit the time-reversed signals. The recompression time is at  $t = 0$  s. Converging and diverging wave fronts appear respectively for negative and positive times. The spatial range around the refocusing point A is  $34 \times 26$  cm<sup>2</sup>. Reprinted (figure) with permission from Ref. [43]. Copyright (2012) by the American Physical Society.

point in Fig. 12.4. With several channels, the PNR increases linearly with the number  $N$  of channels [49]. Although this behavior is expected without damping, it was not obvious to be verified with the typical range of damping of our experiment. The insets of Fig. 12.7

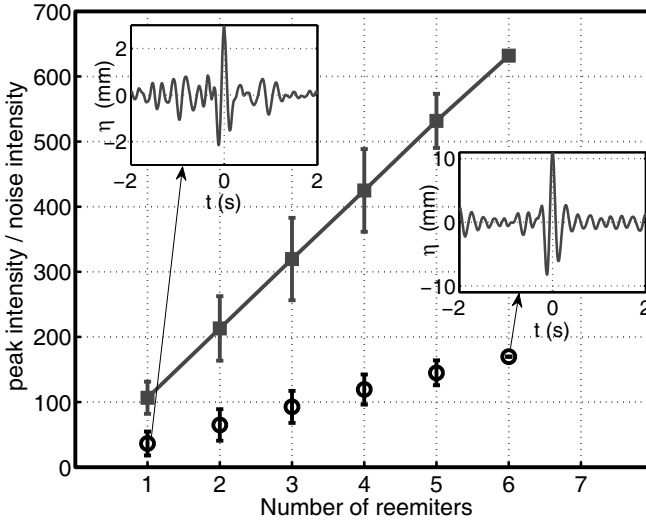


**Figure 12.7** Experimentally measured peak-to-noise ratio as a function of the number  $N$  of channels (black points). For comparison, the blue squares show numerical results with negligible damping. Note the standard deviation accounting for the sensitivity of the refocusing to the position of the reemission point. The insets present the experimental temporal refocalization while using one and six channels. Reprinted (figure) with permission from Ref. [43]. Copyright (2012) by the American Physical Society.

show the temporal recompression for  $N = 1$  and  $N = 6$  at the refocusing point A. The refocusing is clearly visible in the one-channel TR experiment but with higher temporal side lobes than with 6 channels. Note that these temporal signals allow also to define a PNR and we observed that PNR either defined in space or in time have roughly the same values. Varying the damping is more difficult. To perform experiments where the damping effect is negligible would necessitate much larger size of the cavity (e.g., the size of a swimming pool) because the attenuation per wavelength decreases with the frequency [9]. Therefore, numerical simulations have been used to model the case with negligible damping. The results are shown in Fig. 12.7 (blue square) where computations have been done by taking the same protocol as in the experiment. The same trends as in the experiment are observed: i) for  $N = 1$ ,

the PNR is equal to 100 and is given by the number of excited cavity modes that can be resolved in the spectrum in Fig. 12.4, ii) the PNR increases linearly with  $N$ . With about 20 excited modes in our laboratory experiments, versus the 100 modes obtained in the numerics, it appears that the refocusing can be significantly reduced because of the attenuation occurring at that laboratory scale.

Our experiments illustrate the feasibility of a few channel TR refocusing for gravity capillary waves. This has been performed in a well-controlled laboratory context that allows quantitative measurements simultaneously in time and space. At this laboratory scale, with centimetric wavelengths, the quality of the refocusing is limited by the damping due to viscous effects but it is not suppressed. At larger scales, viscous damping highly decreases and numerical simulations show that the refocusing is greatly improved. Thus, this paves the way to applications in the context of water waves in the sea, with very small damping, where very high quality of refocusing is expected.

### 12.3.2 *Time Reversal of Nonlinear Water Waves*

Next, an experimental demonstration of TR of nonlinear waves is presented. Due to the strong nonlinear focusing of NLSE breathers, the doubly localized Peregrine and the higher-order Akhmediev-Peregrine breathers solutions will be used for the demonstration in one spatial direction of wave propagation. Following the 1D NLSE (Eq. 12.44), the experiments, performed in a unidirectional wave basin, are first started by generating the maximal amplitude of hydrodynamic and doubly localized breather by the wave maker, which is considered to be the source of the propagation. Its position is labeled by  $x_S$ . The attenuated breather-type wave field is then measured at the mirror position, labeled by  $x_M$ , after a specific propagation distance. The collected signal is then reversed in time, providing new initial conditions to a wave generator. As for the linear experiment, if the TR symmetry is valid, one should expect the refocusing and the perfect reconstruction of the initial maximal breather compression, after reemitting the time-reversed signal. Due to the experimental limitations with respect to the generation of the time-reversed signal at the mirror position, we will use

the spatial reciprocity of the NLSE in order to reemit the time-reversed surface elevation signal of the attenuated breather from the source and observe the refocusing at the mirror position  $x_M$ , instead of rebroadcasting the reversed wave field from  $x_M$  and expecting refocusing at the source position  $x_S$ .

The experiments are performed in a unidirectional and 15 m long wave flume facility with a constant depth of  $h = 1$  m. A computer-controlled and hydraulic single flap generates surface gravity Stokes waves at one end of the flume at a position we refer to be the source of pulse generation  $x_S$ . A capacitance wave gauge measures the surface elevation along the flume at a position of interest with a sampling frequency of 500 Hz. The wave gauge is placed and fixed 9 m from the wave generator, keeping enough distance from the absorbing beach, which is installed at the other end of the facility in order to avoid wave reflections, which would obviously distort the dynamics of the generated waves. The position of the wave gauge is considered to be the mirror position  $x_M$ . The experimental setup is depicted in Fig. 12.8.

In order to provide ideal experimental conditions, the walls of the flume were therefore properly cleaned and the water was filtered accordingly before performing the experiments in order to minimize the dissipation effects, which have a significant influence on NLSE localized structures, propagating in a water wave flume.

First, the dimensional doubly localized wave profiles of the breathers, satisfying Eq. 12.44, at their maximal amplitude amplification are generated. These initial wave profile amplitudes are amplified by a factor of three for the Peregrine and of five for the Akhmediev–Peregrine solution. The parameters of the corresponding carrier wave have to be carefully chosen in order to



**Figure 12.8** Schematic upper view of the unidirectional wave basin. The single flap, driven by a hydraulic cylinder, is installed at the right end of the wave flume at  $x_S$ . The wave gauge is located at  $x_M$ , 9 m from the wave maker. The absorbing beach is displayed at the left end of the wave facility.

avoid initial wave breaking of obviously strongly nonlinear focused waves at  $x_S$  and in order to reach satisfactory attenuation after 9 m of propagation. Consequently, the carrier wave parameters, determined by the steepness  $\varepsilon$  and the amplitude  $a$ , have to be chosen accordingly. Both parameters are set to be  $\varepsilon = 0.09$  and  $a = 3$  mm for the Peregrine as well as  $\varepsilon = 0.03$  and  $a = 1$  mm for the Akhmediev–Peregrine solution. These chosen steepness values are far from the experimentally determined wave breaking thresholds [50]. The steepness  $\varepsilon$  and the amplitude  $a$  of the Stokes background are sufficient to determine the carrier parameters. Trivially, the wave number is  $k = \frac{\varepsilon}{a}$ . The linear dispersion relation of deep water determine the wave frequency to be  $\omega = \sqrt{gk}$ , while denotes the gravitational acceleration and is  $g = 9.81 \text{ m} \cdot \text{s}^{-2}$ . The initial conditions are then trivially determined by

$$\eta(x^*, t) = \text{Re} (E(x^*, t) \cdot \exp [i (kx^* - \omega t)]), \quad (12.57)$$

evaluated at  $x^* = 0$ , in order to satisfy the maximal breather compression. Figure 12.9 shows the initial conditions applied to the flap at the Position  $x_S$ .

After generating the Peregrine and the Akhmediev–Peregrine breather at their maximal wave amplitude of 0.9 cm and 0.5 cm, respectively, we collect the wave profiles after having being declined in amplitude, as expected and predicted by theory, by use of the wave gauge at  $x_M$ , that is, 9 m from the flap Position  $x_S$ . Here, we notice already a deviation from theoretical weakly nonlinear wave profiles, due to the strongly nonlinear nature of the initially generated wave forms. These discrepancies can be explained by higher-order NLSE, known as the modified NLSE [20]. The corresponding data are shown in Fig. 12.10a,b.

In the third step these recorded breather signals are revised in time. These time-reversed signals provide now new initial conditions to the flap in order to initiate the fourth and penultimate stage of the TR experiment. The latter are depicted in Fig. 12.10c,d. If the considered breather dynamics is indeed TR invariant, it is expected to observe the refocusing of the maximal wave compressions after reemitting the latter time-reversed and slightly modulated signals to the wave maker. Here, we take advantage of the spatial reciprocity of the NLSE equation, thus, we can reemit the

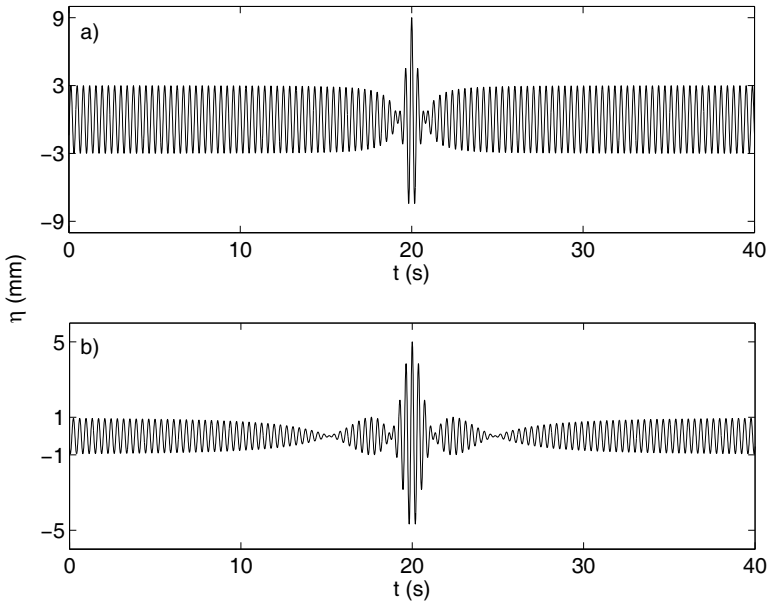


**Figure 12.9** Initial conditions provided by theory (Eq. 12.45) at the position of maximal amplification, that is, at  $X = 0$ , applied to the wave flap at Position  $x_S$ . (a) The carrier parameters for the Peregrine breather-type water wave profile are  $a_0 = 0.3$  cm and  $\varepsilon = 0.09$ . (b) The carrier parameters for the Akhmediev-Peregrine breather-type water wave profile are  $a_0 = 0.1$  cm and  $\varepsilon = 0.03$ .

time-reversed signal from the point  $x_S$  and observe the refocusing at point  $x_M$ , rather than rebroadcasting the reversed wave field from  $x_M$  and expecting refocusing at the position  $x_S$ . At the fifth and last step of the experiments, we measure the surface elevations related to the time-reversed initial conditions, again 9 m from the flap at position  $x_M$ , that is, keeping the wave gauge at the same position. These refocused measurements are compared to the theoretical surface elevations. The corresponding wave profiles are shown in Fig. 12.11.

These results are a clear demonstration of the TR invariance of the hydrodynamic breathers. Clearly, Fig. 12.11 provides an accurate refocusing and reconstruction of the breather surface elevation of the corresponding NLSE solution at its maximal compression, as already presented in Fig. 12.9. The results are in a very good

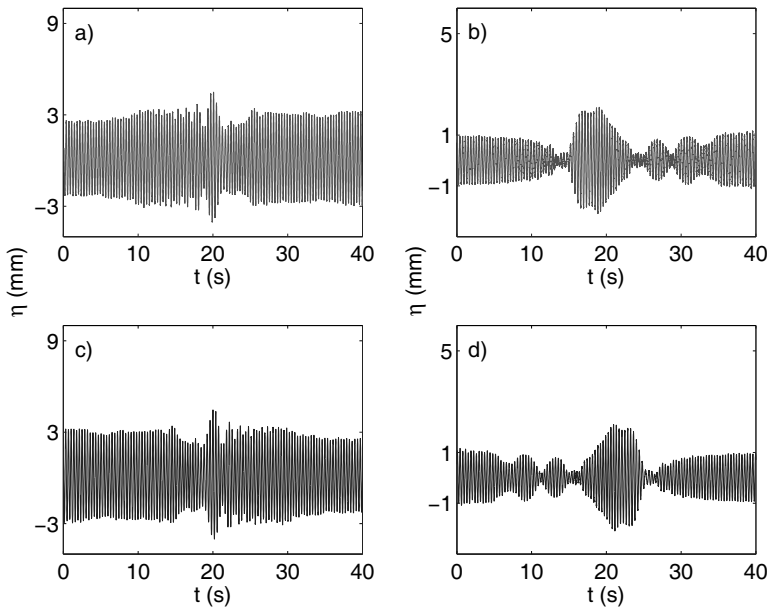


**Figure 12.10** (a) Surface elevation of water wave profile of the attenuated Peregrine breather, recorded at  $x_M$ , located 9 m from the flap. (b) Surface elevation of water wave profile of the attenuated Akhmediev–Peregrine breather, recorded at  $x_M$ , located 9 m from the flap. (c) Time-reversed signal of the measurements shown in (a), providing new initial conditions to the flap and reemitted at  $x_S$ . (d) Time-reversed signal of the measurements shown in (b), providing new initial conditions to the flap and reemitted at  $x_S$ .

agreement with the theoretical predictions, expected at this position within the framework of NLSE. In fact, the maximal water surface amplitude is of 9 mm and of 5 mm for the Peregrine breather and the Akhmediev–Peregrine breather, respectively, which correspond to theoretical values of amplitude amplifications, related to these NLSE solutions at the maximal stage of breather compression and as generated in the first step of the experiment. These observations prove the TR invariance of strongly nonlinear water waves. In addition, these experimental results confirm the accuracy of the NLSE in describing the unidirectional and complex evolution dynamics of rogue waves, taking into account the complex phase-shift dynamics,

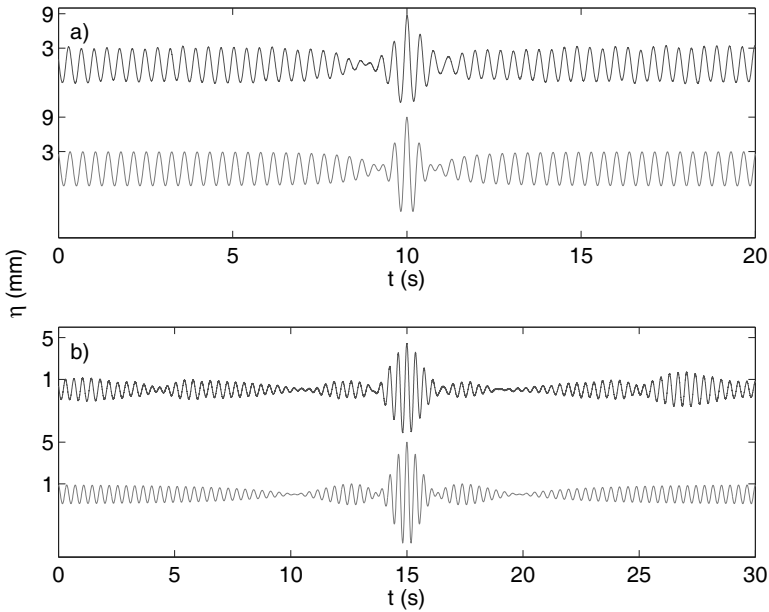


**Figure 12.11** (a) Comparison of the Peregrine surface profile measured 9 m from the paddle at  $x_M$ , while starting its propagation from time-reversed initial conditions (blue upper line) with the expected theoretical NLSE prediction at the same position (red bottom line). (b) Comparison of the Akhmediev–Peregrine surface profile measured 9 m from the paddle at Position  $x_M$ , while starting its propagation from time-reversed initial conditions (blue upper line) with the expected theoretical NLSE prediction at the same position (red bottom line).

related to the modulation instability process. Nevertheless, some discrepancies between theory and experiment can be also noted in terms of asymmetric wave profile shape of the experimental observations, as can be noticed in Fig. 12.11. The latter are due to higher-order nonlinearities (Stokes drift) and to higher-order dispersion effects, not taken into account in the NLSE approach, as well as to occurring experimental imperfections, including dissipation and wave reflection and most importantly noise, naturally and always existing while performing experiments in wave basins. Nevertheless, the experimental observations confirm the possibility to reconstruct strongly localized, thus, strongly nonlinear waves

through TR. Therefore, we emphasize that this technique may be used in order to construct new TR invariant localized structures, described by nonlinear evolution equations, which considerably amplify the amplitude of a wave field, thus, again also in the case of strong nonlinearity.

## 12.4 Discussion and Outlook

Experiments on water wave pulse field reconstruction in the linear and nonlinear regime using TR, provide not only a confirmation of the TR invariance of the hydrodynamic wave motion, but also open new field of possible applications in several dispersive media. This includes, for example, superfluidity [51, 52] and optical fibers [15, 53]. The experiments, involving the doubly localized breather solutions of the NLSE show also limitations, which should be addressed. First, discrepancies with respect to the theoretical NLSE predictions can be noticed. These can be easily explained in view of the natural limitation of the NLSE. A successive analysis could be performed in order to verify the TR invariance, also for higher-order NLSE-type evolution equation [20, 56] as well as within the framework of fully nonlinear equations [55]. This is to accurately characterize possible applications and limitations of the TR method for nonlinear, very steep, and nonbreaking water waves. Another interesting point, which should be addressed from a chaotic dynamics point view is the influence of random noise on the TR reconstruction of NLSE breathers. Next, we inspect the numerical instability of the TR scheme, by perturbing the initial conditions of the same nonlinear experiments within the framework of the NLSE. We used the split-step Fourier method [57, 58] to illustrate the influence of the random noise on the decaying and TR reconstruction dynamics of both, Peregrine and Akhmediev–Peregrine dynamics for the same wave parameters as used in the laboratory experiments. The initial conditions have been multiplied by  $[1 + N\Gamma(t)]$  [59]. Here,  $\Gamma$  is a normally distributed random function, whereas  $N$  denotes the noise level, which is chosen to be  $10^{-1}$  and  $10^{-2}$ , respectively. The numerical results involving the Peregrine breather for the same laboratory parameters over a

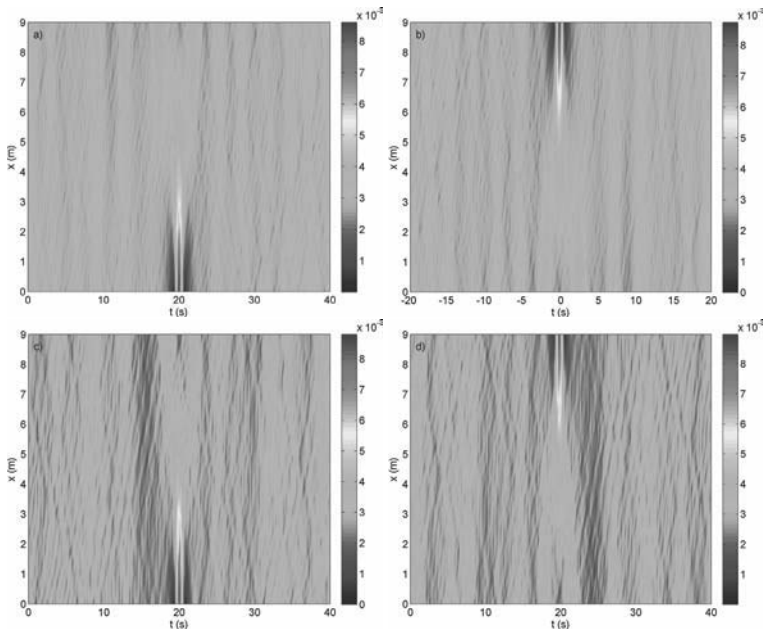


**Figure 12.12** Numerical TR experiment of the Peregrine breather dynamics for  $\varepsilon = 0.09$  and  $a = 3$  mm for two different noise levels using the split-step Fourier method. (a) Decay of the Peregrine pulse from its maximal compression during its evolution over 9 m for a noise level of 10%. (b) Growth of the Peregrine pulse, starting from the time-reversed signal of the experiment (a) at 9 m. (c) Decay of the Peregrine pulse from its maximal compression during its evolution over 9 m for a noise level of 20%. (d) Growth of the Peregrine pulse, starting from the time-reversed signal of the experiment (c) at 9 m.

distance of 9 m are shown in Fig. 12.12a,b for a noise level of  $N = 10\%$  and Fig. 12.12c,d for a considerable noise level of  $N = 20\%$ .

It is noticeable that TR techniques work very well in reconstructing both doubly localized Peregrine-type extreme waves, since the maximal compression of the envelope could be recovered, even in the presence of significant noise. Remarkably, this is also the case for the Akhmediev–Peregrine solution that has a much larger amplitude amplification value and therefore, a more significant nonlinear Stokes wave nature, as shown in Fig. 12.13 (same noise level  $N$  as in the previous figure).

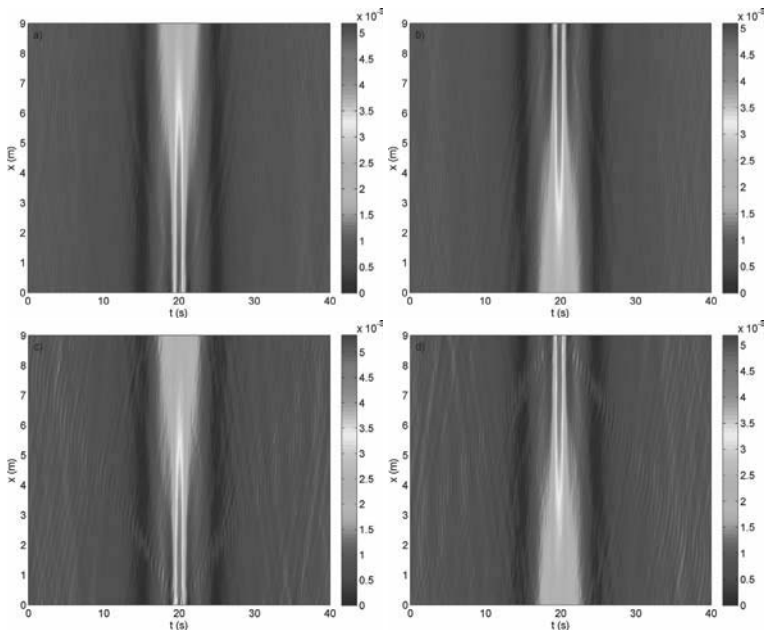


**Figure 12.13** Numerical TR experiment of the Akhmediev–Peregrine breather dynamics for  $\varepsilon = 0.03$  and  $a = 1$  mm for two different noise levels using the split-step Fourier method. (a) Decay of the Akhmediev–Peregrine pulse from its maximal compression during its evolution over 9 m for a noise level of 10%. (b) Growth of the Peregrine pulse, starting from the time-reversed signal of the experiment (a) at 9 m. (c) Decay of the Akhmediev–Peregrine pulse from its maximal compression during its evolution over 9 m for a noise level of 20%. (d) Growth of the Akhmediev–Peregrine pulse, starting from the time-reversed signal of the experiment (c) at 9 m.

Another possible application is the validation of TR reconstruction of nonlinear waves, propagating in two spatial directions [60, 61]. Deep-water evolutions equations, such as the Davey–Stewartson equation [62] or the shallow water KP-I [63] could be used for this investigation. Obviously, experiments for such type of equations are much more difficult to perform. Furthermore, new possible solutions may be derived numerically in the limit of TR convergence.

## 12.5 Conclusion

To summarize, we have discussed the TR invariance of surface gravity water waves in the linear and nonlinear regime. After introducing the governing equations of an ideal fluid and emphasizing the conditions for the TR invariance, we have presented recent experiments, validating the TR approach in reconstructing linear and 2D water pulses, whereas two examples of nonlinear breather-type pulses have been refocused in a 1D water wave flume. The experimental results provide a clear confirmation of the TR invariance of water waves and emphasize novel applications in other dispersive media, such as fiber optics, plasma and Bose-Einstein condensates as well as in remote sensing to name only a few. The effect of dynamical noise on the nonlinear breather wave propagation has been discussed numerically as well. The reported simulations, based on the split-step Fourier method are promising and motivate further analytical, numerical and experimental work in analyzing the hydrodynamics and complex propagation properties of linear and nonlinear waves, using the TR technique.

## References

1. Fink, M. (1997). *Phys. Today*, **3**, 34.
2. Lerosey, G., de Rosny, J., Tourin, A., Derode, A., Montaldo, G., and Fink, M. (2004). *Phys. Rev. Lett.*, **92**, 193904.
3. Fink, M., Cassereau, D., Derode, A., Prada, C., Roux, P., Tanter, M., Thomas, J.-L., and Wu, F. (2000). *Rep. Prog. Phys.*, **63**, 1933.
4. Draeger, C., and Fink, M. (1997). *Phys. Rev. Lett.*, **79**, 407.
5. Feynman, R.P., Leighton, R.B., and Sands, M. (1963). *The Feynman Lectures on Physics*, Vol. I, Chaps. 51–54 (Addison-Wesley, Reading, MA).
6. Roux, P. and Fink, M. (2000). *J. Acoust. Soc. Am.*, **107**, 2418–2429.
7. Ing, R.K. and Fink, M. (1998). *IEEE Trans. Ultrason. Ferroelectr. Freq. Control*, **45**, 1032.
8. Tanter, M., Thomas, J.-L., Coulouvrat, F., and Fink, M. (2001). *Phys. Rev. E*, **64**, 016602.
9. Lighthill, J. (2001). *Waves in Fluids* (Cambridge University Press).

10. Mei, C.C., Stiassnie, M.M., and Yue, D.K.P. (2005). *Theory and Applications of Ocean Surface Waves*, Advanced Series on Ocean Engineering, Vol. 23.
11. Osborne, A. (2010). *Nonlinear Ocean Waves & the Inverse Scattering Transform*, Vol. 97 (Academic Press).
12. Kharif, C., Pelinovsky, E., and Slunyaev, A. (2009). *Rogue Waves in the Ocean* (Springer).
13. Dalrymple, R.A., and Dean, R.G. (1991). *Water Wave Mechanics for Engineers and Scientists* (Prentice Hall).
14. Linton, C.M., and McIver, P. (2001). *Handbook of Mathematical Techniques for Wave/Structure Interactions* (CRC Press).
15. Remoissenet, M. (1999). *Waves Called Solitons* (Springer).
16. Debnath, L. (1994). *Nonlinear Water Waves* (Academic Press).
17. Stokes, G.G. (1847). On the theory of oscillatory waves, *Trans. Camb. Philos. Soc.*, **8**, 441–455.
18. Benjamin, T.B. and Feir, J.E. (1967) The disintegration of wave trains on deep water. Part 1. Theory, *J. Fluid Mech.*, **27**, 417–430.
19. Zakharov, V.E. (1968). Stability of periodic waves of finite amplitude on a surface of deep fluid, *J. Appl. Mech. Tech. Phys.*, **9**, 190–194.
20. Dysthe, K.B. (1979). Note on the modification of the nonlinear Schrödinger equation for application to deep water waves, *Proc. R. Soc. A*, **369**, 105–114.
21. Zakharov, V.E. and Shabat, A.B. (1972). Exact theory of two-dimensional self-focusing and one-dimensional self-modulation of waves in nonlinear media, *J. Exp. Theor. Phys.*, **34**, 62–69.
22. Besselov, V.I., and Talanov, V.I. (1966). Filamentary structure of light beams in nonlinear liquids, *JETP Lett.*, **3**, 307–310.
23. Lake, B.M., and Yuen, H.C. (1977). Note on some nonlinear water-wave experiments and the comparison of data with theory, *J. Fluid Mech.*, **83**, 75–81.
24. Benjamin, T.B. (1967). Instability of periodic wavetrains in nonlinear dispersive systems, *Proc. R. Soc. A.*, **299**, 59–75.
25. Zakharov, V.E. and Ostrovsky, L.A. (2009). Modulation instability: the beginning, *Physica D*, **238**, 540–548.
26. Hasimoto, H., and Ono, H. (1972). Nonlinear modulation of gravity waves, *J. Phys. Soc. Jpn.*, **33**, 805–811.
27. Yuen, H.C., and Lake, B.M. (1982). Nonlinear dynamics of deep-water gravity waves, *Adv. Appl. Mech.*, **22**, 67–229.

28. Tulin, M.P., and Waseda, T. (1999). Laboratory observations of wave group evolution, including breaking effects, *J. Fluid Mech.*, **378**, 197–232.
29. Akhmediev, N., Eleonskii, V.M., and Kulagin, N. (1985). Generation of periodic sequence of picosecond pulses in an optical fibre: exact solutions, *J. Exp. Theor. Phys.*, **61**, 894–899.
30. Akhmediev, N., and Korneev, V.I. (1986). Modulation instability and periodic solutions of the nonlinear Schrödinger equation, *Theor. Math. Phys.*, **69**, 1089–1093.
31. Kuznetsov, E.A. (1977). Solitons in a parametrically unstable plasma, *Sov. Phys. Dokl.*, **22**, 507–508.
32. Ma, Y.C. (1979). The perturbed plane wave solutions of the cubic nonlinear Schrödinger equation, *Stud. Appl. Math.*, **60**, 43–58.
33. Peregrine, D.H. (1983). Water waves, nonlinear Schrödinger equations and their solutions, *J. Aust. Math. Soc. Ser. B*, **25**, 16–43.
34. Akhmediev, N., Ankiewicz, A., and Soto-Crespo, J.M. (2009). Rogue waves and rational solutions of the nonlinear Schrödinger equation, *Phys. Rev. E*, **80**, 026601.
35. Akhmediev, N., Ankiewicz, A., and Taki, M. (2009). Waves that appear from nowhere and disappear without a trace, *Phys. Lett. A*, **373**, 675–678.
36. Dudley, J.M., Genty, G., Dias, F., Kibler, B., and Akhmediev, N. (2009). Modulation instability, Akhmediev breathers and continuous wave supercontinuum generation, *Opt. Express*, **17**, 21497.
37. Kibler, B., Fatome, J., Finot, C., Millot, G., Dias, F., Genty, G., Akhmediev, N., and Dudley, J.M. (2010). The Peregrine soliton in nonlinear fibre optics, *Nat. Phys.*, **6**, 790–795.
38. Chabchoub, A., Hoffmann, N.P., and Akhmediev, N. (2011). Rogue wave observation in a water wave tank, *Phys. Rev. Lett.*, **106**, 204502.
39. Chabchoub, A., Hoffmann, N., Onorato, M., and Akhmediev, N. (2012). Super rogue waves: observation of a higher-order breather in water waves, *Phys. Rev. X*, **2**, 011015.
40. Bailung, H., Sharma, S.K., and Nakamura, Y. (2011). Observation of Peregrine solitons in a multicomponent plasma with negative ions, *Phys. Rev. Lett.*, **107**, 255005.
41. Onorato, M., Proment, D., Clauss, G., and Klein, M. (2013). Rogue waves: from nonlinear Schrödinger breather solutions to sea-keeping test, *PLOS ONE*, **8**, e54629.

42. Chabchoub, A., Kibler, B., Dudley, J.M., and Akhmediev, N. (2014). Hydrodynamics of periodic breathers, *Phil. Trans. R. Soc. A*, **372**, 20140005.
43. Pr zadka, A., Feat, S., Petitjeans, P., Pagneux, V., Maurel, A., and Fink, M. (2012). TR of water waves, *Phys. Rev. Lett.*, **109**, 064501.
44. Chabchoub, A., and Fink, M. (2014). Time-reversal generation of rogue waves, *Phys. Rev. Lett.*, **112**, 124101.
45. Maurel, A., Cobelli, P., Pagneux, V., and Petitjeans, P. (2009). *J. Appl. Opt.*, **48**, 380; Cobelli, P., Maurel, A., Pagneux, V., and Petitjeans, P. (2009). *Exp. Fluids*, **46**, 1037.
46. Recent improvements of the technique for signal processing and the choice of painting particles can be found, respectively, in G. Lagubeau et al., in preparation; Pr zadka, A., Cabane, B., Pagneux, V., Maurel, A., and Petitjeans, P. (2012). *Exp. Fluids*, **52**, 519.
47. Cobelli, P., Petitjeans, P., Maurel, A., Pagneux, V., and Mordant, N. (2009). *Phys. Rev. Lett.*, **103**, 204301.
48. Cobelli, P., Pagneux, V., Maurel, A., and Petitjeans, P. (2009). *Europhys. Lett.*, **88**, 20006; (2011). *J. Fluid Mech.*, **666**, 445–476.
49. Draeger, C., and Fink, M. (1999). *J. Acoust. Soc. Am.*, **105**, 611.
50. Chabchoub, A., Hoffmann, N., Onorato, M., Slunyaev, A., Sergeeva, A., Pelinovsky, E., and Akhmediev, N. (2012). Observation of a hierarchy of up to fifth-order rogue waves in a water tank, *Phys. Rev. E*, **86**, 056601.
51. Gross, E.P. (1961). Structure of a quantized vortex in boson systems, *Il Nuovo Cimento*, **20**, 454–457.
52. Pitaevskii, L.P. (1961). Vortex lines in an imperfect Bose gas, *Sov. Phys. JETP*, **13**, 451–454.
53. Dudley, J.M., Dias, F., Erkintalo, M., and Genty, G. (2014). Instabilities, breathers and rogue waves in optics, *Nat. Photon.*, **8**, 755–764.
54. Craig, W., Guyenne, P., and Sulem, C. (2010). Hamiltonian approach to nonlinear modulation of surface water waves, *Wave Motion*, **47**, 552–563.
55. (2013). On the highest non-breaking wave in a group: fully nonlinear water wave breathers versus weakly nonlinear theory, *J. Fluid Mech.*, **735**, 203–248.
56. Craig, W., Guyenne, P., and Sulem, C. (2010). Hamiltonian approach to nonlinear modulation of surface water waves, *Wave Motion*, **47**, 552–563.
57. Hardin, R.H., and Tappert, F.D. (1973). *SIAM Rev. Chronicle*, **15**, 423.

58. Fisher, R.A., and Bischel, W.K. (1975). *Appl. Phys. Lett.*, **23**, 661 (1973); *J. Appl. Phys.*, **46**, 4921.
59. Chen, S., Soto-Crespo, J.M., and Grelu, P. (2014). Dark three-sister rogue waves in normally dispersive optical fibers with random birefringence, *Opt. Express*, **22**, 27632–27642.
60. Waseda, T., Kinoshita, T., and Tamura, H. (2009). Evolution of a random directional wave and freak wave occurrence, *J. Phys. Oceanogr.*, **38**, 621–639.
61. Toffoli, A., Gramstad, O., Trulsen, K., Monbaliu, J., Bitner-Gregersen, E., and Onorato, M. (2010). Evolution of weakly nonlinear random directional waves: laboratory experiments and numerical simulations, *J. Fluid. Mech.*, 313–336.
62. Davey, A., and Stewartson, K. (1974). On three dimensional packets of surface waves, *Proc. R. Soc. A*, **338**, 101–110.
63. Kadomtsev, B.B., and Petviashvili, V.I. (1970). On the stability of solitary waves in weakly dispersive media, *Sov. Phys. Dokl.*, **15**, 539–541.



# Taylor & Francis

Taylor & Francis Group

<http://taylorandfrancis.com>